The Electrochemical Society
Advancing solid state & electrochemical science & technology

ACCEPTED MANUSCRIPT • OPEN ACCESS

Investigating the Performance and Safety of Li-Ion Cylindrical Cells Using Acoustic Emission and Machine Learning Analysis

Investigating the Performance and Safety of Li-Ion Cylindrical Cells Using Acoustic Emission and Machine Learning Analysis

SCHOLARONE™
Manuscripts

Investigating the Performance and Safety of Li-Ion Cylindrical Cells Using Acoustic Emission and Machine Learning Analysis

Arthur Fordham,[1,2,=] Seung-Bin Joo,[2,3,=] Rhodri E. Owen,[1,2,3] Elias Galiounas,[1] Mark Buckwell,[1,3] Dan J. L. Brett,[1,2] Paul R. Shearing,[2,4 5] Rhodri Jervis,[1,2,z] and James B. Robinson[1,2,3,z]

[1] Electrochemical Innovation Lab, Department of Chemical Engineering, University College London, London WC1E 7JE, UK

[2] The Faraday Institution, Quad One, Harwell Science and Innovation Campus, Didcot OX11 0RA, UK

[3] Advanced Propulsion Lab, Marshgate, University College London, London E20 2AE, UK,

[4] Department of Engineering Science, University of Oxford, Oxford OX1 3PJ, UK

[5] ZERO Institute, Holywell House, Osney Mead, University of Oxford, Oxford OX2 0ES,UK

=These authors contributed equally to this work.

[z]E-mail: rhodri.jervis@ucl.ac.uk; j.b.robinson@ucl.ac.uk

Abstract

Acoustic emission (AE) is a low-cost, non-invasive, and accessible diagnostic technique that uses a piezoelectric sensor to detect ultrasonic elastic waves generated by the rapid release of energy from a localised source. Despite the ubiquity of the cylindrical cell format, AE techniques applied to this cell type are rare in literature due to the complexity of acoustic wave propagation in the architecture alongside the challenges associated with sensor coupling. Here, we correlate the electrochemical performance of cells with their AE response, examining the differences during pristine and aged cell. AE data was obtained and used to train binary classifiers in a supervised setting, differentiating pristine from aged cells. The best accuracy was achieved by a deep neural network model. Unsupervised machine learning (ML) models, combining dimensionality reduction techniques with clustering, were also developed to group AE signals according to their form. The groups were then related to battery degradation phenomena such as electrode cracking, gas formation, and electrode expansion. There is the potential to integrate this novel ML-driven approach for widespread cylindrical cell testing in both academic and commercial settings to help improve the safety and performance of lithium-ion batteries.

1. Introduction

In an era marked by unprecedented reliance on portable electronic devices, extensive electrical power networks, and the accelerating integration of electric vehicles (EVs) into our daily lives, the demand for battery technologies has increased significantly in recent years. In the automotive sector, global lithium-ion battery (LIB) demand has seen an annual rise of 65%, growing from 330 GWh in 2021 to 550 GWh in 2022.[1] Moreover, global renewable energy capacity is at an all-time high at 440 GW in 2023 as efforts are made to shift towards renewable energy sources, such as solar photovoltaic cells and wind power.[1] Consequently, the role of batteries in grid-scale energy storage is not only essential but is expected to grow in importance with international initiatives such as Net Zero Emissions by 2050.

As batteries become ubiquitous across transportation, stationary, and consumer electronics applications, it is paramount that methods to monitor the safety and performance of batteries are developed. Manufacturing defects,[2] mechanical loading,[3] electrical abuse,[4] and exposure to external heat can result in battery failure, which in turn poses a significant chemical and fire hazard.[5,6] The Electrical Power Research Institute evidenced in June 2021 that, in the span of four years, over 30 large-scale battery energy storage sites globally suffered failures which caused destructive fires.[7] With transportation electrification, EV battery fire incidents have consistently occurred and shown to lead to injuries and, in extreme cases, casualties.[8–10] Even in non-flaming battery failures, toxic and flammable gases, such as hydrogen fluoride (HF), cyanide, carbon dioxide (CO_2), carbon monoxide (CO), and hydrogen (H_2), can vent, further increasing the risk of explosion and human exposure.[3]

Battery monitoring methods are a crucial first line of defence against such failures. Among the multitude of existing battery diagnostic techniques, acoustic emission (AE) monitoring is a recently developed technique which enables low-cost and non-invasive analysis of batteries. AE techniques use a piezoelectric sensor to passively detect transient elastic waves generated from localised energy releases caused by battery degradation phenomena, such as electrode cracking, deformation, and gas evolution.[11]

This study combines AE techniques with machine learning (ML) analysis to monitor the state-of-health (SoH) and degradation in cylindrical cells. Cylindrical cells have benefits relative to other cell formats, namely pouch and prismatic cells, in terms of their mechanical stability due to even distribution of internal pressure build-up and slower failure propagation in multi-cell battery modules[12] thanks to air-filled gaps between individual cells which reduce thermal contact.[13] These advantages, paired with the suitability of cylindrical cells for automated manufacturing, means that they are widely deployed in devices such as laptops, power tools and electric vehicles.[14]

While acoustic techniques for pouch and prismatic cells have been relatively extensively studied, research on AE with cylindrical cells is currently limited due to the complex acoustic wave propagation behaviour in the layered "*jelly-roll*" structure of a cylindrical cell.[15] The speed of an acoustic wave depends on several factors, including the elastic modulus and density of the medium. Within any kind of cell, there are layers of various materials, such as $LiCoO_2$, graphite, Al, Cu, PVDF and carbon black, each with different densities and elastic moduli. As an acoustic pulse travels through the multi-material stack, each time it encounters a material interface a fraction of the pulse transmits, the remaining fraction reflects, and subsequently numerous pulses constructively or destructively interfere with one another.[16] As a result, the acoustic behaviour rapidly becomes more complex, especially since commercial cylindrical cell designs typically consist of 15 to 25 windings of these layers.[17] Additionally, the curved geometry of cylindrical cells causes more complex internal scattering effects on transient elastic waves (**Figure 1**). The fact that the density and elastic modulus of the cell change

2

depending on the local state-of-charge (SoC),[18] the multitude of curved layers within a cylindrical cell, the reflections between dozens of material interfaces, and the interference between waves all contribute to AE techniques with cylindrical cells being notoriously difficult.
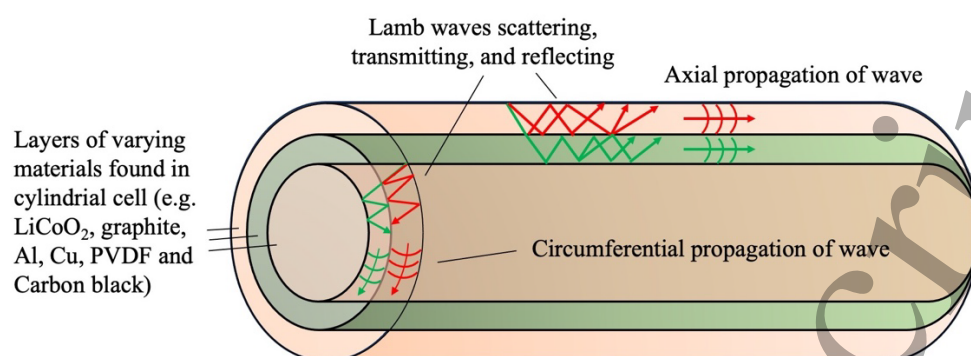

Figure 1. Simplified visualisation of Lamb waves propagating axially and circumferentially in a cylindrical cell. The figure demonstrates the difficulty of acoustic analysis due to various wave phenomena that occur inside the cylindrical geometry.

AE Techniques with Cylindrical Cells

Despite challenges, several studies have shown that AE techniques can be effective with cylindrical cells. In 2010, Komagata *et al.* showed that when cycling 18650 cylindrical LIBs, most AE signals were detected in the same region of the voltage profile: at 20-40% and 0-20% SoC during discharge.[19] It was theorised that the occurrence of these AE signals was caused by volume change induced fracture of $LiCoO_2$. Moreover, model half-cells were also tested, and AE data was correlated to the cells' degradation as AE events during discharge primarily occurred after 50 cycles, i.e., when the cell's discharge capacity began declining. More recently, Zhang *et al.* built upon such existing works by more precisely estimating the SoH of 18650 cylindrical LIBs using AE detection.[20] Two types of AE signals with distinct frequency spectrums were detected: *'continuous'* AE signals, which were regular, sinusoidal, and attributed to electrode expansion, electrochemical reaction, and gas generation, and *'pulse-type'* AE signals, which decayed rapidly, and were attributed to electrode cracking. Zhang *et al.* were able to determine SoH by following the decrease in the amplitudes of dominant frequency peaks of continuous AE signals during discharge. Additionally, the observation that the number of pulse-type AE signals was largest in the early cycles, declined sharply, maintained a stable low, then gradually increased (at around 300 to 400 cycles) was also used to estimate SoH. Zhang *et al.* performed their cycles in two batches of tests with different C-rates and the acoustic behaviour changed depending on this, stressing the importance of considering cycle parameters and history of a battery when attempting to accurately monitor SoH.

Although acoustic emission (AE) has been utilised to monitor cylindrical cells, research on abuse and safety testing is still in its early stages. Consequently, there are significant gaps in the literature that need to be addressed. Previous work using AE has only looked at mechanical abuse and stems from related tests in fields where the use of AE is more established such as metallurgy. Hao *et al.* demonstrated that AE techniques could be used to analyse mechanical damage to 18650 cylindrical LIBs.[21,22] Cells were subjected to *in situ* 3-point bending tests while voltage data was collected alongside AE data. Four stages of the bending process were identified using a force-displacement diagram: inter-electrode gap squeezing and layered electrode debonding; electrode layer slipping; continuation of electrode layer debonding and plastic deformation; and, finally, electrode cracking and maximum plastic deformation. The distinct behaviour of the number of AE hits and unique frequency spectrums

3

of AE signals from each stage were used to determine the extent of mechanical failure. Researching an acoustic method which accurately characterizes the damage of LIBs and using it to supplement existing battery management systems is significant since, for example, electrochemical data has been shown to be ineffective in detecting mechanical failure.[23] Furthermore, Hao *et al*. developed their work and correlated the AE measurements to three-dimensional digital image correlation (3D-DIC), and thermal imaging methods for cylindrical cells at different SoC while the cells underwent mechanical abuse bending loads.[21] They observed that the bending modulus and stiffness of the battery increased with the increase of SoC. The results demonstrated that none of the cells' voltage or temperature changed during the entire bending process meaning no short circuit occurred. A significant limitation is that the paper only investigates a cell at constant SoC, which is unrealistic for cells being used in real-life EV applications.

Tang *et al*., followed up previous works by adding ML cluster analysis to similar experiments to understand the signals attributed to the damage types.[23] The authors again used a 3-point bending mechanical abuse method on cylindrical 18650 cells and used AE to monitor the damage. The statistical-based factor analysis (FA) and the fuzzy clustering method (FCM) characterized the AE signals of various damage types. This machine learning clustering tool observed that the cracking of electrodes and separators occurred later than delamination and interlayer slippage. Delamination-related signals were found to have a higher frequency component than the other two damage types. FA and FCM were effective at studying the mechanical damage types of LIBs as well as the expansion processes of various damage types. To summarise, the utilisation of AE during the electrochemical cycling of cylindrical cells remains largely unexplored. However, it holds the promise of yielding valuable insights due to its connection with various outputs of battery performance, emphasising the significance of our research efforts in this area.

Alongside AE, ultrasonic testing (UT) is an acoustic diagnostic technique, but that which involves an externally generated signal produced from a piezoelectric transducer in contact with a cell.[11] This signal is propagated through the material before being recorded either by the same transducer via the reflection of the signal in the material or by another transducer attached to the opposite surface of the cell. The technique allows analysis of the internal structure of the system because acoustic wave propagation is affected by the condition of the battery material. UT has also led to the successful monitoring of SoH of cylindrical LIBs. Hsieh *et al*. used electrochemical-acoustic time-of-flight (EAToF) experiments to detect degradation in LIBs.[16] Acoustic time-of-flight (ToF) maps during cycling were obtained and plotted along with other information, such as total reflected and transmitted signal amplitudes. Around the first 11 cycles, the total reflected signal and transmitted signal intensities changed significantly as a function of SoC, but after this initial period, the values stabilized, suggesting the presence of a formation period. Moreover, after around 27 cycles, high-intensity peaks emerged in the ToF map in the 8-12 microseconds region. The unique behaviour of ToF maps and total reflected and transmitted signal amplitudes demonstrated that UT may be a powerful diagnostic technique for battery health monitoring. This research, however, could be extended by relating certain acoustic behaviour to individual physical effects. Ultrasonic ToF maps provide information regarding the chemical and structural composition of a material such as a battery[11,24–26]. For example, the density and Young's modulus change at different states-of-charge can be detected and are well documented. These techniques, when complemented by electron, neutron, or X-ray interrogation methods, can improve our understanding of ToF analysis and physical changes within cells.[27] Applying similar UT techniques to cylindrical cells has yet to be applied and would be promising for SoH monitoring. Like AE methods, they operate at a fraction of the cost, are non-invasive and can be readily applied to off-the-shelf commercial batteries.

4

This work presents a systematic investigation into how the SoH of a cell affects the type of acoustic signal released. The data collected was fed into machine-learning algorithms, which were used to classify the SoH of batteries based on AE signals. The results would have a role to play in developing cylindrical cell diagnostic techniques and improving battery safety and performance for both the academic and commercial communities.

2. Methodology

2.1 Experimental Setup

Molicel 21700 P42A cylindrical cells were secured in a bespoke holder, as shown in **Figure 2**, with acoustic couplant (Olympus H-2 couplant) applied on the battery-slider and slider-sensor interfaces. To optimise acoustic transmission, the slider's base was designed with a curvature to ensure complete contact with the cylindrical cell. The acoustic sensor (NANO 30 Sensor Mini, 300 kHz, resonant, 1M cable, BNC connector, Mistras) was securely positioned at three distinct points along the slider, specifically marked at 18, 36, and 54 mm in relation to the negative tab. This arrangement facilitated a comprehensive acoustic mapping across the cylindrical cell, allowing for the identification of varying signals at each position during electrochemical cycling. A Gamry Instruments Interface 5000E potentiostat was used to perform electrochemical cycling on the cell. The AE data was obtained by connecting the piezoelectric acoustic sensor to a pre-amplifier followed by a computer with AEwin acoustic signal processing software (1283-7001-ACQ-KEY-SW AEwin for USB software and 1 (USB key-based) acquisition licence. Through initial calibration laboratory tests, a 29 dB amplitude threshold and 2000 μs pre-trigger were determined to be ideal for capturing most AE signals produced by the cell while ensuring background noise was minimised.

2.2 Data Collection and AE Analysis

Two pristine Molicel 21700 P42A cylindrical cells at 100% SoH and two aged cells at 80% SoH were tested. The aged cells reached 80% SoH after 800 cycles at a rate of 1C. For each cell, 10 cycles of constant-current charge-discharge between 2.5 and 4.2 V were completed at the 18 mm sensor position. Subsequently, the acoustic sensor was moved to the 36 mm position, where the cell was subjected to 10 cycles, and afterwards moved again to the 54 mm position for a further 10 cycles. Each cell was then cycled for 100 further cycles with the AE sensor at each position, after the initial data acquisition, to investigate the effects of an ageing cell on the acoustic signals *in operando*. The aim of shifting the sensor was to examine the effect of sensor position on the AE waveforms, as well as to limit experimental bias. Without sensor shifting, the disparity between AE signals from different cells may be attributed to experimental conditions, such as material surface conditions, quality of couplant application, ambient temperature, and minor manufacturing differences in cell construction. Sensor shifting ensures that there is some variation of the above conditions in every cell's acoustic dataset. This makes it more likely that when training a machine learning model to differentiate between pristine and aged cells, they will be differentiated because of some ageing characteristics they have and not because of coincidental experimental biases. In essence, sensor shifting is an attempt to reduce the probability of overfitting to the experimental conditions. Moreover, with sensor shifting, it is possible to determine where certain signals originate from by probing three positions along the cell. The data collection protocol is displayed in **Table 1**. While data from four cells were collected in this study, our future work will conduct more experiments with cells at varying SoH, aiming to gather larger data sets.

5

AE signals with an amplitude over 29 dB were registered by the AEwin software and labelled as *"hits"*. 29 dB was decided as the amplitude of background noise in the laboratory based off preliminary experiments without any battery cycling. A preset threshold of 29 dB in the software was set to exclude the background noise while recoding any signal above this amplitude. For each AE hit, the raw waveform data from the piezoelectric sensor (2000 data points in time) was recorded, and 14 significant acoustic parameters of the AE signal (Rise Time, Counts to Peak, Energy, Duration, Amplitude, Average Frequency, RMS, ASL, PCNTS, Threshold, Reverberation Frequency, Initiation Frequency, Signal Strength, Absolute Energy) were calculated. The time-domain waveform data were further processed through bespoke Python code, which obtained the digital Butterworth band-pass filtered signal (50 kHz – 1MHz) and the frequency spectrum via Fast Fourier Transform (FFT). Moreover, amplitude and cumulative absolute energy (CAE) from the acoustic hit features dataset were plotted and analysed alongside the electrochemical cycling data.
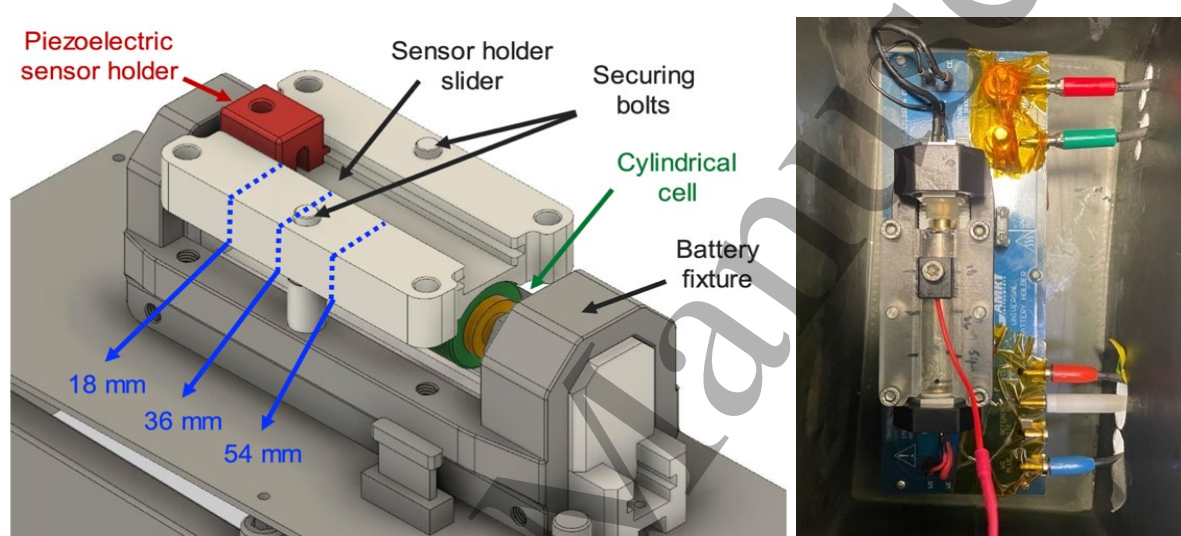
Figure 2. AE signal acquisition hardware setup: labelled CAD model (left) and final experimental setup (right). Each part of the experimental set up is labelled. The piezoelectric acoustic sensor was connected to a filter, amplifier, AEwin Node, and computer for signal processing.

Table 1. Data collection protocol for each cell tested. Cell 1 and Cell 2 were pristine and Cell 3 and Cell 4 were aged.

	State of Health	C-Rate	Number of cycles at 18 mm	Number of cycles at 36 mm	Number of cycles at 54 mm
Cell 1	100%	C/3	10	10	10
Cell 2	100%	1C	10	10	10
Cell 3	80%	C/3	10	10	10
Cell 4	80%	1C	10	10	10

2.3 Supervised ML Framework

The supervised ML framework aimed to use the 14-dimensional acoustic parameter dataset (obtained from cycling described in Section 2.2) to train a model for binary classification of AE hits (excluding background noise AE signals) between pristine and aged cell signals. AE signals are complex and rich in information, but difficult to interpret manually. Therefore, a blackbox statistical approach was hypothesised to be able to encounter patterns that are non-obvious in the data and draw correlation between the complex signal output as the battery SoH.

Three supervised ML models were constructed, tested, and compared: Logistic Regression, a Support Vector Machine (SVM), and a Deep Neural Network (DNN). The DNN could also be referred to as a Feed-Forward Neural Network (FFNN) since it is not a convolutional NN, or a recurrent NN but we refer to this model as DNN throughout the study. For all three models, the acoustic features dataset was standardised to zero mean and unit variance. An 80-20 training-test split was applied for the logistic regression and SVM models. For the DNN model a validation set was also held out, leading to a 64-16-20 training-validation-test split of the data. As one of the simplest binary classification algorithms, the logistic regression model acted as a baseline with which comparisons could be made. SVM was chosen as a more complex second model because of its suitability with smaller datasets. Kernelised SVM algorithms transform lower-dimensional data into a higher-dimensional space and find hyperplanes which optimally split and classify the data. We used a radial basis function (RBF) kernel, with the associated gamma parameter set to 0.2. It is the use of a kernel (RBF in this case) which achieves the transformation to higher dimensional space. Without it, SVM would operate in the original space and draw a boundary through it. The gamma parameter controls the range of influence of individual data points on the decision boundary. A lower gamma implies that individual instances have a larger range of influence, leading to a smoother decision boundary. In the limit, this can lead to results similar to a linear model. A higher gamma decreases the range of influence of individual instances, leading to a more irregular decision boundary. In the limit, the boundary can wiggle around individual instances. Setting gamma to 0.2 indicates that the RBF kernel is configured with a moderate level of influence from individual data points. Lastly, for the DNN model, an 80-20 training-validation split was further applied to enable validation loss tracking to prevent overfitting. The model was trained to 1000 epochs with batch size set to 32. An early stopping mechanism monitored validation loss with a patience of 150 epochs to halt training in the case of overfitting. Regarding experimental setup, recording AE signals at three positions along the cell via different sensor placement was the main practical attempt to avoid overfitting in the training dataset. Architecturally, the DNN consisted of a 14-dimensional input layer and a 1-dimensional output layer with a sigmoid activation function, hence producing a 0 and 1 output for aged and pristine predictions, respectively. Three hidden layers were constructed with RELU activation functions with 11, 8, and 5 nodes, respectively. The model calculated binary cross entropy loss and used the *Adam* optimiser. Plots of training and validation loss minimisation are shown in **Figure 3.**
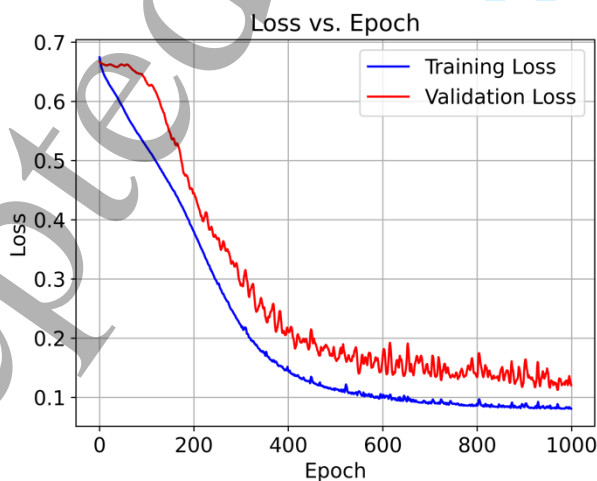

Figure 3. Training and validation loss plotted against epochs, demonstrating the DNN fitting to the AE dataset.

7

2.4 Unsupervised ML Framework

The unsupervised ML framework aimed to gain a deeper understanding of the AE signals by categorising them according to acoustic properties. In reference to Table 1, data from the pristine cells (Cell 1 and Cell 2) were used. AE hits (including background noise AE signals that exceeded the threshold) from cycling pristine cells were analysed by applying dimensionality reduction to the dataset, plotting the transformed data in an easily visualisable 3D plot, and applying k-means clustering. This is an unsupervised clustering algorithm where the number of clusters must be predetermined. Instances are then placed into clusters so that inter-point distances are small compared with data-points that lie outside the cluster. Each AE waveform has two different datasets that could be used for the above process: the 14-dimensional acoustic features data and the 2000-dimensional time-domain waveform data. Furthermore, each standardised dataset could be processed using two different dimensionality reduction algorithms: principal component analysis (PCA) and autoencoders. The four groups of datasets and dimensionality reduction techniques are summarised in **Table 2** and the results from each group were compared against one another. The latent space of the autoencoder consists of 5 dimensions, but since we cannot visualise 5-dimensional data, we extracted the first three dimensions for 3D plots. Nonetheless, when running k-means clustering on the data points in the latent space, the k-means clustering algorithm runs on the 5-dimensional data, so the clustering process *does* consider the ways in which the data points vary in all five dimensions.

Table 2. A table summarizing the datasets and dimensionality reduction techniques used for unsupervised ML. Data from Cell 1 and Cell 2 (Table 1) were used to form these groups.

	Dataset	Dimension of original dataset	Dimension of reduced dataset	Dimensionality reduction method	Clustering algorithm
Group 1	Acoustic features	14	3	PCA	k-means
Group 2	Acoustic features	14	5	Autoencoders	k-means
Group 3	Time-domain waveform	2000	3	PCA	k-means
Group 4	Time-domain waveform	2000	5	Autoencoders	k-means

PCA is a common dimensionality reduction technique that linearly transforms the original dataset into a lower dimensional space while maintaining most of the variation of the data. This technique is accomplished by placing a constraint on the subspace being sought, which must comprise orthonormal basis vectors. It can be shown that the resulting basis vectors are the eigenvectors of the covariance matrix of the original dataset, which can be trivially computed. Their ordering, in terms of explainable variance, is the ordering of the respective eigenvalues. To aid visualisation, the first 3 principal components were selected. This was applied to two datasets, one comprising the 14 acoustic features and the other comprising entire time-domain waveforms. Both the acoustic features and time-domain waveform dataset were standardised before applying PCA to reduce data into three dimensions. For each case, the explained variance ratio (the amount of variance of the original dataset explained by the three principal components) was computed through the Python Scikit Learn library and used to quantify the performance of PCA.

In comparison, autoencoders are unsupervised neural networks that reduce dimensionality through non-linear transformation. Autoencoders have an encoder-decoder structure with a middle "bottleneck" layer called the latent space, as shown in **Figure 5**. The bottleneck layer forces the original data to be compressed into a lower dimensional space. The autoencoder is trained to reconstruct the input layer (which contains the original data) at the output layer by minimising the reconstruction error,

8

i.e. the error between the input and output layer. PCA operates by projecting original data onto a set of orthogonal axes. In this sense the features of the original dataset are linearly combined, and the transformation overall is considered linear. On the other hand, autoencoders have the capacity to learn non-linear relationships between datapoints and leverage those in applying a non-linear transformation reducing dimensionality. They can capture complex relationships and project data onto non-linear manifolds in the latent space, allowing them to represent data in a way that may not be achievable with a linear technique such as PCA. Empirical testing was used to find the best results. An autoencoder with 14-11-8-5-8-11-14 nodal architecture and RELU activation functions was found to be ideal for the above datasets. We iterated through different architectures and hyperparameters to find the configuration that best suits these datasets. The initial 14 nodes correspond to the input layers that match the dimensionality of the data (14 AE parameters). The architecture is symmetric around the bottleneck layer, which has 5 nodes. Symmetry in the encoder-decoder structure often helps in learning a more effective representation. The decreasing number of nodes towards the bottleneck layer (14-11-8-5) indicates the progressive reduction in dimensionality leading to the latent space. The increasing nodes in the decoder (8-11-14 nodes) mirrors the encoder, but in reverse order. The primary purpose of the bottleneck layer is to compress the input data into a lower-dimensional representation. This reduction in dimensionality helps in capturing the most essential features of the data while discarding less relevant or redundant information. The use of a bottleneck or a lower-dimensional latent space in autoencoders is not universally better than other architectures; it depends on the specific requirements and characteristics of the problem. Nonetheless, the inclusion of a bottleneck layer has certain advantages that make it a common and effective choice in various scenarios. Mean squared error (MSE) loss was used as the loss function paired with the *'Adam'* optimiser. In **Figure 4**, three random instances are presented to elucidate the autoencoder's performance on signals sourced from the acoustic features dataset. Prior to training, the autoencoder exhibited no ability to reconstruct the original data. However, after training, the model successfully reconstructs the original signal, as shown by the overlap of the reconstructed signal with the original in Figure 4. The overlap indicates that the lower-dimensional latent space effectively captures the key attributes of the original dataset. We note that there is a small mismatch in the 'count-to-peak', data point and this could be due to several factors. The training data might not cover all signal variations, leading to gaps in the model's learning. The autoencoder's complexity might be insufficient to capture detailed features, and dimensionality reduction may cause the loss of specific features such as 'count-to-peak.' The model will continue to be developed in future following further experiments and data collection from different degraded cells will lead to an improved overlap between signals.
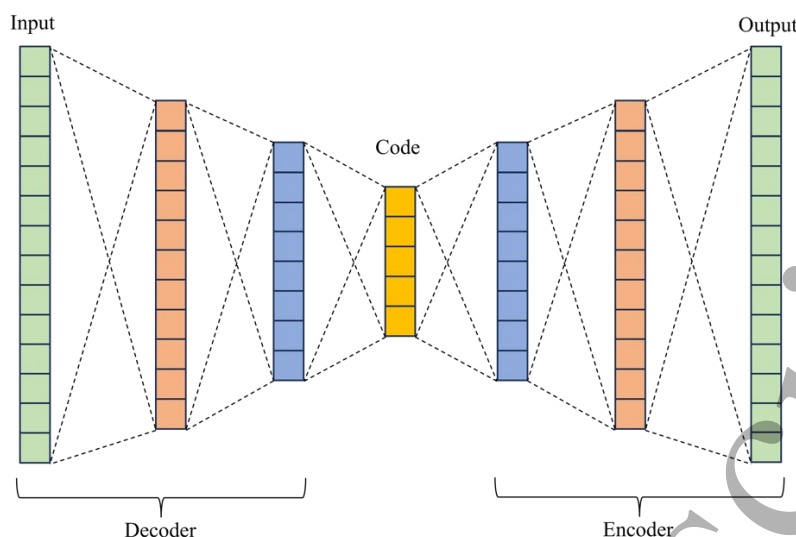
Figure 4. "Bottleneck" structure of the autoencoder neural network (14-11-8-5-8-11-14) used in the analysis. The primary purpose of the bottleneck layer is to compress the input data into a lower-dimensional representation. This reduction in dimensionality helps in capturing the most essential features of the data while discarding less relevant or redundant information. The use of a bottleneck or a lower-dimensional latent space in autoencoders is not universally better than other architectures; it depends on the specific requirements and characteristics of the problem. Nonetheless, the inclusion of a bottleneck layer has certain advantages that make it a common and effective choice in various scenarios.

After dimensionality reduction, k-means clustering was used to group AE waveforms into clusters. Silhouette score and qualitative graphical analysis determined the selection of the parameter k, i.e. the number of clusters to be generated. The silhouette score is a metric that characterises the clustering performance by measuring the average similarity of data points to same-cluster points and comparing this to the similarity of data points to other-cluster points. The scores range from -1 to +1, where -1 implies the sample may be incorrectly clustered, 0 suggests the sample is on the decision boundary between adjacent clusters, and +1 indicates the sample is distant from neighbouring clusters. For Group 1 (acoustic features dataset with PCA), clustering results for various k values are shown in **Figure *6*(a)**. Five, six, and seven clusters clearly show points in separate clusters being close to one another, indicating suboptimal grouping. This is corroborated by **Figure 6(b),** which shows silhouette scores below 0.5 for $k = 5, 6, 7$. The choice between two, three and four clusters was more ambivalent, and thus, qualitative decisions were made. The two clusters option was eliminated as it yielded trivial groups, where most signals were in one cluster and the outliers in the other. The four clusters option ($k = 4$) was chosen over three clusters as it better segmented the inverted V-shaped structure into three distinct sections (and an additional cluster for distant outliers) while also exhibiting a marginally higher silhouette score. A similar analysis was completed for all four dataset groups (Table 2) in the unsupervised ML framework when determining the parameter k for clustering. As with PCA, we applied k-means clustering to the reduced 5-dimensional dataset derived from the latent space of the trained autoencoder.
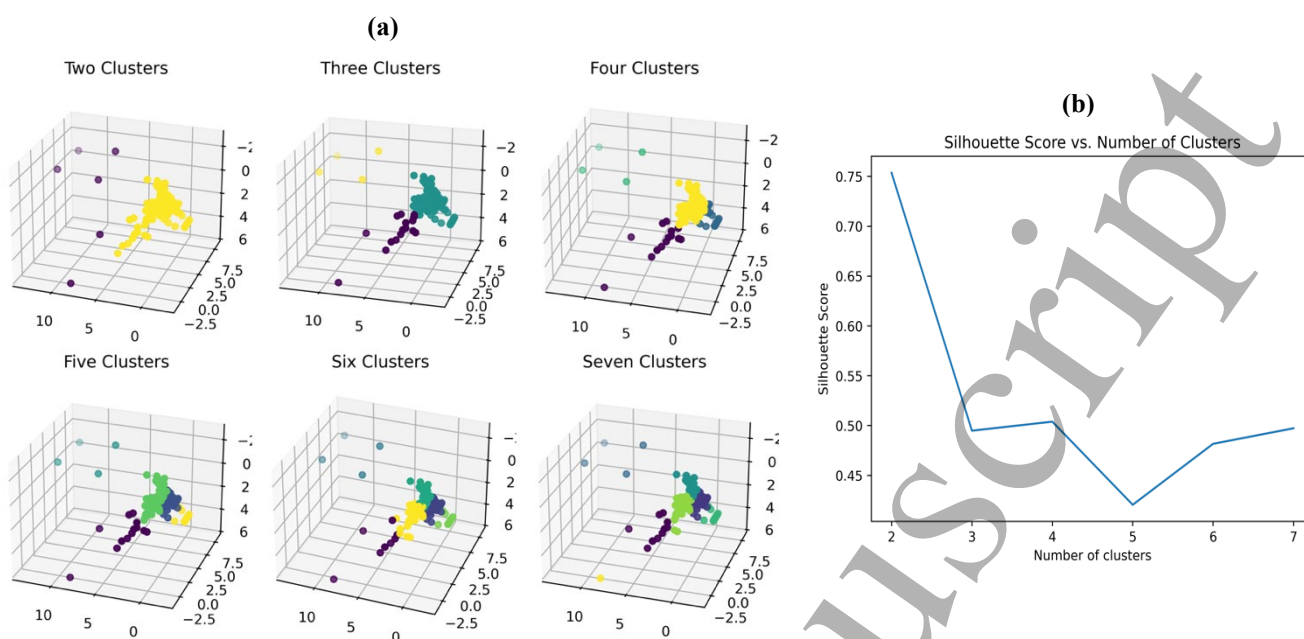
Figure 5(a). Three-dimensional plots in principal component space showing Group 1 clustering results for various k values: k = 2, 3, 4, 6, 7. **(b)** Plot of silhouette score vs. k value, i.e., number of clusters.

2.5 X-ray Computed Tomography Measurements

The internal structure of each cell used in this investigation was scanned using X-ray Computed Tomography. Each cell was scanned twice using a lab-based X-ray CT instrument (Nikon XT 225, Nikon Metrology, UK). The first scan was prior to cycling and the second was after cycling. Cells were held using a 3D-printed holder fabricated by a 3D printer (Ultimaker S3, UK). The voltage and beam current were set at 150 kV and 150 µA, respectively, resulting in a power of 22.5 W. A cone-beam employing a tungsten target was used with an exposure time of 1 s per projection, and a total of 3185 projections were collected per tomogram with a 0.5 mm Sn filter. The scans took approximately 25 minutes each. The scans were then reconstructed using Nikon CT Pro 3D software (Version XT 4.4.4, Nikon Metrology, Tring, UK). The Gabor filter was applied to improve the contrast of raw images before further segmentation and final 3D visualization (Avizo 2019.4, Thermo-Fisher Scientific, USA).

3. Results and Discussion

3.1 AE Analysis Results

For the initial experiments, we cycled each cell (referred to as Cell 1, Cell 2, Cell 3, and Cell 4 in Table 1) a total of 10 times at three different locations of the AE transducer (located at 18mm, 36mm, and 54mm along the cell), as illustrated in Figure 2. Consequently, each cell underwent a total of 30 cycles during these specific experiments. AE hits and corresponding electrochemical cycling data for Cell 1 (C/3 C-rate and pristine cell at 100% SoH) are shown in **Figure 7**, and the remaining processed data figures for Cells 2, 3 and 4 can be found in Supplementary Information. For all four cells, the transducer position did not illustrate a consistent effect on the occurrence, frequency, or pattern of AE hits and CAE jumps across the initial 10 cycles. Comparing C/3 and 1C results, no clear pattern was found as to how C-rate affects AE amplitude and CAE behaviour. Furthermore, the type of AE waveform, i.e. pulse-type signal as shown in **Figure 7(h)** or continuous-type signal shown in **Figure**

11

7(i), and the AE signal's frequency spectrum had no correlation with SoC, transducer position, or C-rate during the 10 cycles of testing.
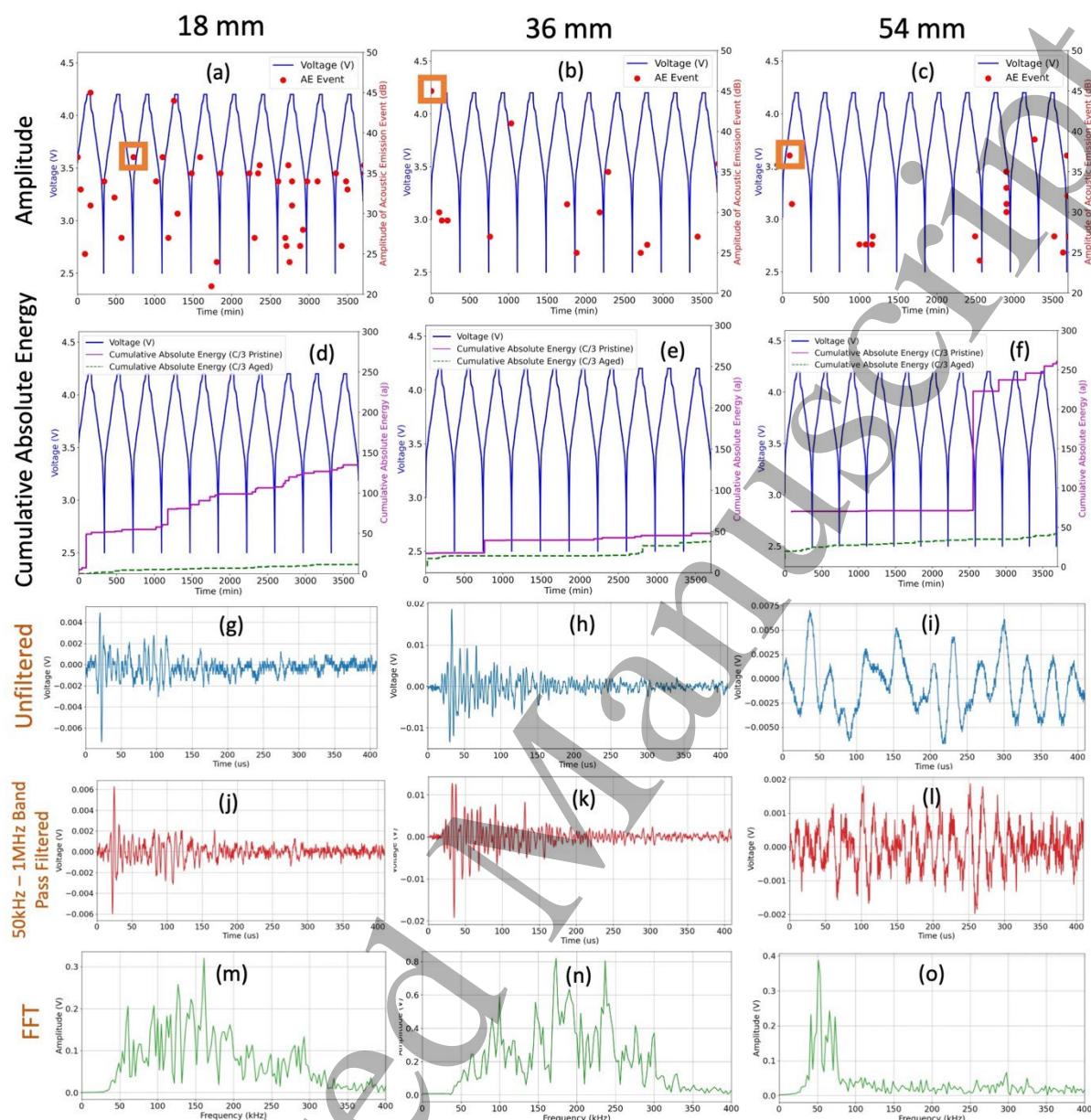

Figure 6. Cycling data for Cell 1 (C/3 pristine cell). Each column represents a transducer position (18, 36, or 54 mm). Row 1 shows plots of voltage as the cell repeatedly charges and discharges (blue), alongside the amplitude of AE hits represented by red points. Row 2 shows plots of voltage once again, but with CAE as a step plot. In this row, the CAE for Cell 3 (aged) are also shown in green dashed lines since a comparison is made in the next paragraph. Row 3 shows the raw time-domain AE waveforms of sample hits that are encircled in row 1 plots with an orange square. Rows 4 and 5 show the band pass filtered signal and FFT signal, respectively, of raw waveforms in row 3.

However, when comparing aged (displayed in the Supplementary Information) and pristine cell signals (Cell 1 vs Cell 3), pristine cell cycling exhibited significantly more CAE jumps exceeding 15 aJ. Across all cycling experiments on the aged cell, there was 1 CAE jump over 15 aJ in magnitude. In contrast, across the pristine cell cycling runs, 11 CAE jumps with magnitudes greater than 15 aJ were observed. Moreover, CAE jumps from aged cell signals never exceeded 15 aJ, whereas the maximum CAE jump recorded from pristine cells was 180 aJ, as shown in **Figure 7(f)**. While the distinctive behaviour of CAE jumps for cells at different SoH is useful, it alone is insufficient to rapidly determine

12

the SoH of the cell as CAE jumps are relatively rare and irregularly occur in the span of 10 cycles. Further long-term cycling with *operando* AE monitoring in Section 3.5 will investigate the changes in AE signal as degradation develops within the internal structure. Another consistent observation was that in various pristine and aged cell cycling runs, there were regular AE hits of similar amplitudes at the 2.5 V point of the voltage cycle, where discharge to charge transition occurs. These regular waveforms generally shared a distinct sustained pulse shape shown in **Figure 7(g)**, and reviewing the relevant literature, is likely attributed to cracking at the bottom of discharge[28–34] due to mechanical stress during cycling, and is attributed to electrode material expansion and repeated cycling-induced degradation. This macro cracking predominantly occurs in the negative electrode (anode) but can also affect the positive electrode (cathode) or interfaces. Schweidler *et al.*[33,34] and Choe *et al.*[30] verified the nature of these acoustic signals as cracks by categorising them into clusters according to their frequencies and employing ex-situ Scanning Electron Microscopy (SEM) on both electrodes. Unlike in previous work, we employ techniques such as X-ray Computed Tomography here, discussed in the Section 3.3, to help to understand the physical origin of the signals further in a non-destructive manner.

3.2 Supervised ML Results

In the previous section, the AE results were interpreted qualitatively and manually, which led to difficulty in determining obvious trends within the data. This issue highlighted the necessity to invoke machine learning algorithms to process and classify the data more effectively, which in turn could then be used for AE monitoring of cylindrical cells in the future more generally. As we will go on to show in this section, application of ML models allowed these trends and conclusions to become clear.

In the analysis of Figures 7, S1, S2, and S3, a total of 246 AE signals were examined, with 125 originating from pristine cells and 121 from aged cells. Of these, 86 signals were identified and removed as background noise, leaving 160 signals for model analysis. Notably, logistic regression, SVM, and DNN models all effectively distinguished between AE signals from aged and pristine cells. The performance evaluation of these models is illustrated in **Figure 8** through a confusion matrix. In the test data, 32 signals were utilised, representing 20% of the 160 total signals in the combined training and test sets. The DNN exhibited the highest accuracy of 93.8% when classifying the unseen test dataset. This was followed by the SVM and logistic regression models, with accuracies of 71.9% and 68.8%, respectively. Both models commonly misclassified AE hits from the aged cell as pristine cell signals, doing so with 21.9% of the test dataset. While the DNN was the most computationally expensive model to train of the three, on average training the neural network using the Python TensorFlow library on a computer with a 2.6 GHz quad-core Intel Core i7 could be completed in under 15 seconds. Thus, for practical applications, the DNN is equally as suitable to use as a rapid binary diagnostic technique for gauging SoH by passing AE signals through the trained model in real-time.
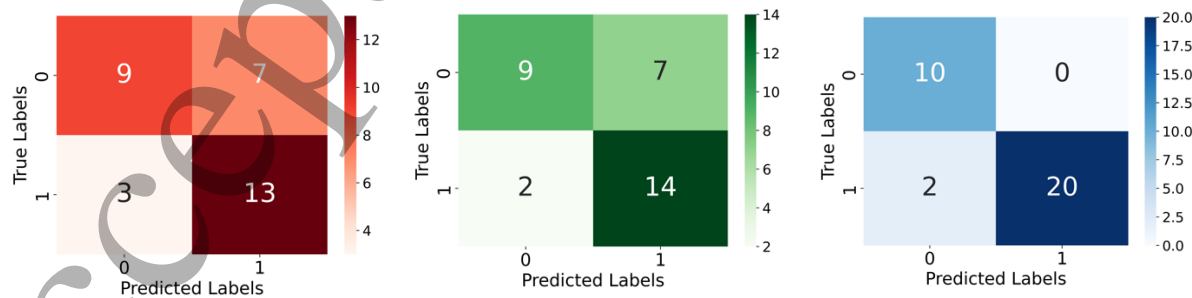

Figure 7. Confusion matrices for logistic regression (left), SVM (middle), DNN (right) models on the test dataset (pristine = 1, aged = 0).

The DNN used the initial 10 cycles worth of AE data from each transducer position to classify each cell. The model was able to accurately distinguish between pristine (Cell 1 and 2) and aged cell (Cell 3 and 4) signals produced over the initial testing of 10 cycles at each transducer position, suggesting that SoH decline measurably affects the inherent AE signal behaviour. Further long-term continuous AE monitoring experiments over more electrochemical cycles (explored in Section 3.5) would reveal how AE signals incrementally change after each cycle as SoH gradually decreases further. Both short-term and long-term experiments have benefits for understanding the role of AE in monitoring the SoH of batteries. Short-term experiments provide a smaller and more limited dataset for electrochemical performance and AE activity analysis. However, it also means our classifier's successful results are more meaningful because it is a more rapid diagnostic technique that does not require thousands of cycles to reveal useful observations. Many existing AE papers using pouch cells monitor SoH but some of these patterns arise after hundreds of cycles.[20,35] In contrast, supervised ML models identify aged from pristine cell signals with 10 cycles of acoustic data in our work.

3.3 Unsupervised ML Analysis Results

Group 1 (PCA with acoustic features dataset) and Group 2 (autoencoder with acoustic features dataset) were the two most successful methods in effectively clustering the pristine cell AE signals into meaningful groups of distinct acoustic properties. For the unsupervised ML analysis, all signals from the pristine cells (125 AE signals) were used for the analysis. The 3D plots of the resulting clusters are visualised in **Figure 9** PCA of the acoustic features dataset revealed an inverted V-shaped structure where its vertex and two 'legs' constituted three clusters and the relatively distant outliers were a separate cluster. Due to their stochastic nature, autoencoders gave a different mapping of points onto the latent space representation each time the neural network was trained with a random initialisation. We did generate a two-dimensional dataset using a dimensionality reduction method and applied *k*-means clustering to compare with the 3-dimensional dataset plotted in Figure 9. However, through iterative processing and plotting in different dimensions, we determined that the explanations and 3-dimensional plots in Figure 9 best represented the data. When PCA was performed to reduce the dimensions to 3, the explained variance ratio was 0.753827, meaning 25% original dataset's variance was lost. Reducing the dimensions to 2 resulted in a significantly lower explained variance (0.5230) ratio and a greater loss of original data, which we wanted to avoid. Moreover, a PCA in 4 dimensions would prohibit the visualisation of all the principal components at once. Similarly, based on empirical observations, autoencoder analysis with reduced dimensions (2, 3, or 4) showed poor reconstruction, meaning that a reduction to 5 dimensions was chosen. The latent space of the autoencoder consists of 5 dimensions, but since we cannot visualise 5-dimensional data, we extracted the first three dimensions. These three dimensions are plotted in **Figure 9 (right)**. Nonetheless, when running k-means clustering on the latent space, the algorithm operates on 5-dimensional data, considering variations across all five dimensions during the clustering process.
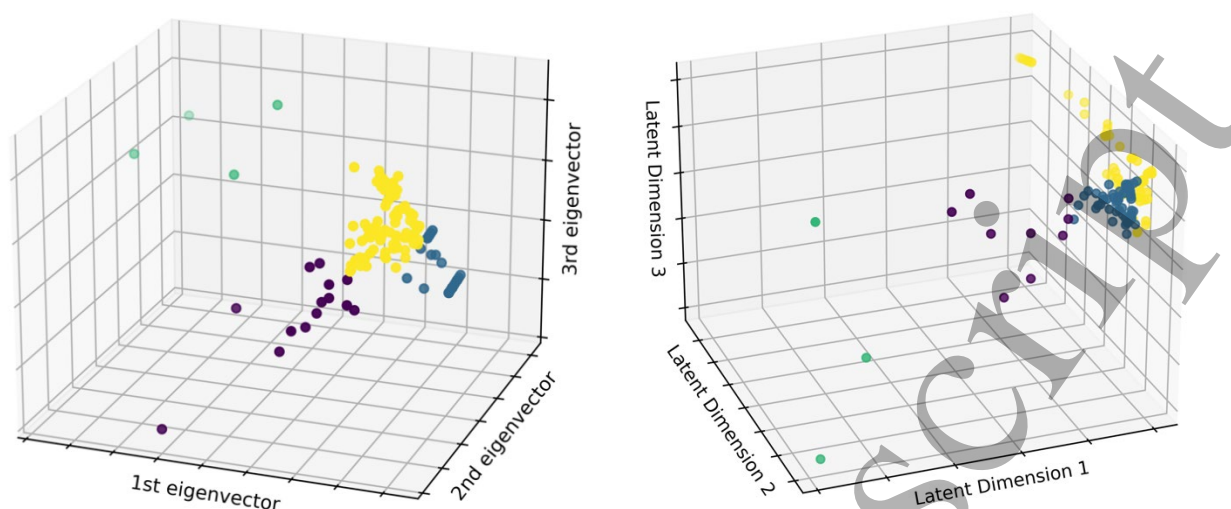
14

Figure 9. 3D plots showing k-means clustering results after applying PCA (left) and autoencoder neural networks (right) to the 14-dimensional acoustic features dataset. Each colour represents a different cluster.

Group 1 and 2 methods labelled AE waveforms into clusters of distinct acoustic properties as tabulated in **Table 3** (same group terminology as in Table 2). Two main types of signals were observed: pulse-type signals with a sharp peak and decay, and continuous-type signals with longer duration and more regular sinusoidal shapes. While pulse-type signals were significantly more common than continuous-type signals, both unsupervised ML methods categorised pulse-type and continuous-type signals into different clusters. Moreover, points within the same cluster had similar orders of magnitude for peak amplitude, allowing for the distinction between high amplitude and low amplitude pulse-type signals, which generally lay in the 0.006 – 0.02 V and 0.001 – 0.004 V range, respectively. Background noise signals were not removed from the dataset in the hope that the unsupervised models would cluster noise signals into a separate cluster. However, analysing the results, noise signals seemed to be distributed among various clusters with no clear pattern. The clustering shown in **Figure 9** can be incorporated into a workflow to monitor degradation in cylindrical LIBs *in situ*. This would correlate AE events to degradation phenomena by combining dimensionality reduction with clustering and classification. Previous works by Zhang *et al.* have also similarly distinguished between pulse-type and continuous signals, attributing the former to electrode cracking and the latter to gas formation and electrode expansion.[20] A complete workflow would involve using a pretrained model for dimensionality reduction, followed by *k*-means clustering, followed by the clusters being human-labelled as in this work. A classifier can be subsequently trained, post-labelling, to automate the attribution of degradation modes to new AE signals. During operation, newly recorded signals are transformed into latent space and classified by the classifier. The advantage of reducing the dimensionality is that new signals can be plotted together with the training clusters, allowing the visual inspection of the classifier's output.

Group 3 (PCA with time-domain waveform dataset) and Group 4 (autoencoder with time-domain waveform dataset) were unsuccessful as reducing 2000-dimensional data into three dimensions led to excessive information loss. For PCA, the explained variance ratio was low at 0.442, and although the reduced dimension was raised to 10 dimensions to compensate, the explained variance ratio was still poor, and the resultant clustering showed low silhouette scores. The suboptimal performance of the autoencoder is shown in the Supplementary Information (**Figure S4**), where after training, the autoencoder fails to reconstruct the original signals, indicating that the latent space was not representative of the original input data. This was corroborated by the validation loss during training,

which as shown in **Figure S5**, failed to decrease and converge. The architecture of the neural network was varied by adding hidden layers, enlarging existing hidden layers, and increasing the size of the latent space layer; however, this made no significant improvements and the final clustered data continued producing low silhouette scores.

We used 125 signals in the unsupervised analysis. In future work, we will conduct more experiments with cells at varying states of health (SoH) to gather larger data sets. Additionally, to determine the origin of each signal and the corresponding clustering for labelling, we will perform further tests in future work on cells undergoing specific mechanical and electrochemical processes. For example, we will attach a sensor to a cell during its formation cycle, when substantial gassing occurs as the Solid Electrolyte Interphase (SEI) develops on the anode. The signals produced during formation cycle, caused by gassing, will be analysed, and compared to signals from degradation studies. Furthermore, we will induce rapid degradation using aggressive rates and voltage ranges known to cause cracking and electrode stress. The signals from these experiments, likely to be 'pulse-type', can be compared to those in this manuscript. Analysing these signals and developing confirmed labels for each signal type within the ML model will further enhance our understanding of cell longevity and battery safety. This approach will address various cell degradation mechanisms, including mechanical and electrochemical degradation.

Table 3. Table summarising general trends in acoustic properties of AE signals from each cluster for both the PCA and autoencoder techniques. Although the table shows characteristics of most AE signals from a particular cluster, there were outlier signals within each cluster which did not correspond to these results. Group 1 and 2 are taken from Table 2.

	Cluster 1	Cluster 2	Cluster 3	Cluster 4
Group 1 (PCA + *k*-means clustering)	High amplitude (6-20 mV) pulse-type signal E.g. Figure 7(h), Figure S3(h) in Supplementary Information.	Noise signals & low amplitude (1 – 4 mV) pulse-type signal E.g. Figure 7(g), Figure S2(i) in Supplementary Information.	Noise signals & low amplitude (1 – 4 mV) pulse-type signal E.g. Figure 7(g), Figure S2(i) in Supplementary Information.	Continuous-type signal E.g. Figure 7(i), Figure S1(h), Figure S2(h) in Supplementary Information.
Group 2 (Autoencoders + *k*-means clustering)	High amplitude (6 – 20 mV) pulse-type signal E.g. Figure 7(h), Figure S3(h) in Supplementary Information.	Noise signals, pulse-type signals of widely varying amplitudes	Continuous-type signal & high amplitude (6 – 20 mV) pulse-type signal E.g. Figure 7(i), Figure S1(h) and Figure S2(h) in Supplementary Information.	Noise signals & low amplitude (1 – 4 mV) pulse-type signal E.g. Figure 7(g), Figure S2(i) in Supplementary Information.

3.4 X-ray Computed Tomography

This study employed X-ray CT analysis, using the Nikon XTH 225, to scrutinise the impact of internal structural degradation on the acoustic emission (AE) signals of aged and pristine cylindrical cells. The key finding was the pronounced deformation of electrodes within the aged cell, primarily concentrated in the inner layers, presenting a stark contrast to the relatively intact structure of the pristine counterpart (**Figure 10**). This deformation led to the emergence of inter-electrode gaps and a

16

notable distortion in electrode geometry. Such internal degradation has been seen previously by Kok *et al.*[36,37] and other authors in different cells (after more cycle than 1000 cycles) and would likely contribute to changes in AE signal. [38–42]The degraded structural features likely altered various acoustic wave scattering, reflection, and transmission effects, manifesting as discernible disparities in AE signal characteristics between the aged and pristine cells. This elucidates a relationship between internal structural degradation, specifically electrode deformation, and a cell's AE signal properties. Moreover, it is well documented in the literature that cracks and gas evolution developing in a degrading cell also lead to acoustic signals of particular frequencies.[29,34,43–47] This underscores the potential of accurate AE signal interpretation for monitoring cell structural integrity during aging and thus is promising for enhancing diagnostic techniques in the field of energy storage and battery health assessment. X-ray CT is one of many methods of understanding the physical origin of the acoustic signals observed.[48] Future work will explore additional correlative techniques to enhance our understanding of the origins of AE signals in batteries.
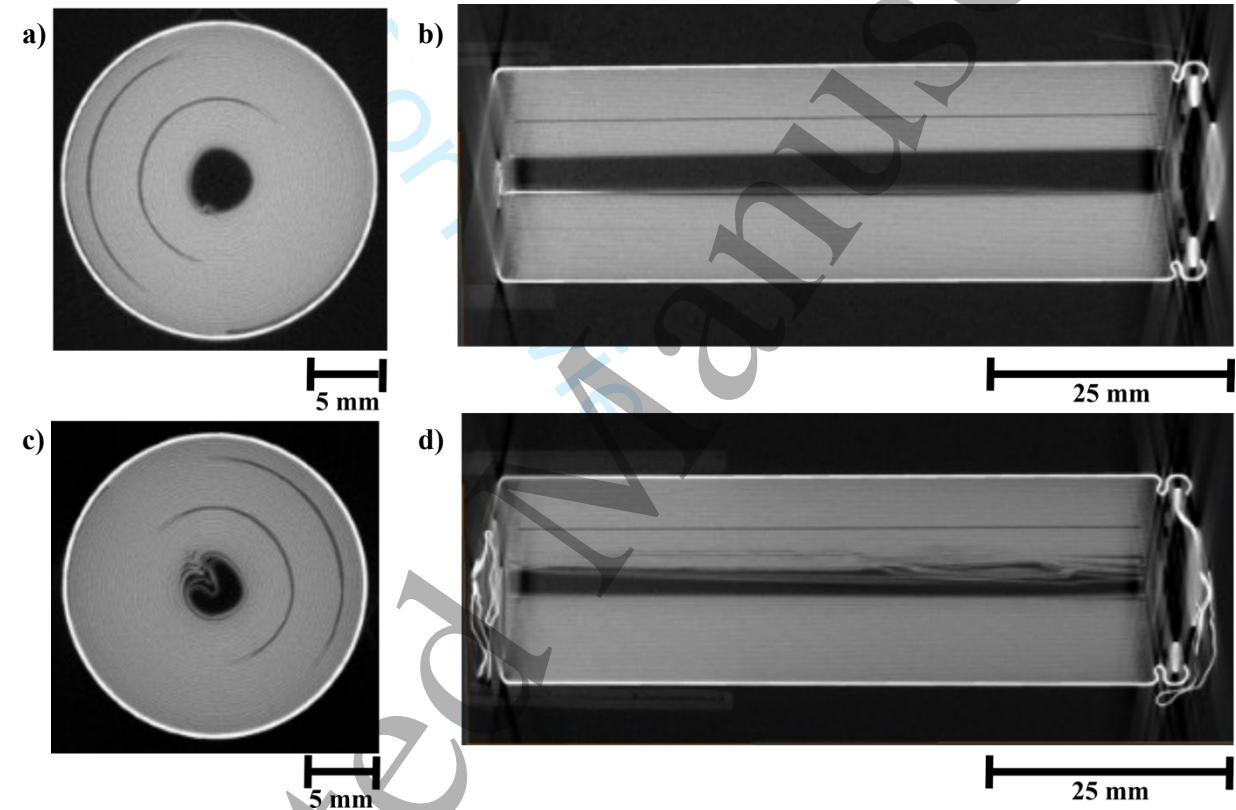

Figure 10. Nikon XTH 225 X-ray CT scans of pristine (a-b) and aged (c-d) cells. XY plane scans are shown on the left, and XZ plane scans are shown on the right. Scale bars are displayed below each sub-figure. Deformation in the aged scan relative to the pristine can be clearly seen in both the XY and XZ geometries. Degradation is a likely cause in the difference in observed waveforms between the two cells.

3.5 Long-term Acoustic Emission Monitoring

All previous results discussed were derived from AE signals obtained during the experiments conducted on Cells 1-4. As shown in Table 1, Cells 1 and 2 were in their pristine condition, and Cells 3 and 4 were aged (80 % SoH after 1000 cycles) before this experiment. These cells were cycled 10 times at each of the three acoustic transducer positions along the cell (a total of 30 cycles during AE testing). However, further long-term AE monitoring while the cell is cycled, can produce data that would allow the model to investigate a more gradual change in AE signals during SoH deterioration.

17

Thus, following the preliminary 10 cycles at each acoustic transducer position, a more extensive cycling experiment was conducted spanning 100 cycles at the 54 mm transducer position, while monitoring AE signals. The 54 mm transducer position was chosen since it was where the most interesting AE activity was observed during the preliminary experiments. Long-term AE tests were run for both a pristine cell (Cell 1) and an aged cell (80% SoH) (Cell 3).

As shown in **Figure 11**, throughout 100 cycles, the pristine cell produced fewer hits overall (224 AE hits) compared to the aged cell (336 AE hits). All 560 AE hits (including potential background noise signals) were used to train and test the same DNN classifier discussed in Section 3.2. Despite the presence of background noise, aged and pristine cell signals were effectively distinguished with an accuracy of 85.8% (confusion matrix is shown in **Figure S7**). The increased occurrence of acoustic events in the aged cell, as compared to the pristine cell, can be attributed to the progressive degradation of internal components during extended cycling. The prolonged cycling induces mechanical stresses, microstructural changes, and chemical transformations within the cell, leading to heightened acoustic emissions. The elevated number of acoustic hits in the aged cell, as evidenced by the 336 AE hits compared to the pristine cell's 224 AE hits over 100 cycles, signifies an intensified internal activity and structural evolution. This phenomenon serves as a valuable indicator for assessing the state-of-health (SoH) and elucidating the intricate mechanisms associated with degradation in batteries, providing crucial insights for diagnostic purposes in battery performance monitoring. In contrast, for the preliminary experiments, we saw that there was higher CAE for pristine after 10 cycles than aged. We note that while CAE and frequency of AE hits are correlated, they are not the same measurement and can show differing trends.

To extend the analysis, we built a neural-network regression model (which takes the acoustic features as the input) in the hope of being able to predict the cycle number, given the AE signal. The neural network regression model utilised the same 80-20 training to test split and the same 14-11-8-5-1 nodal architecture as the DNN in Section 3.2., but the final layer used a linear activation function instead of a sigmoid activation function. This function allows the model to output over an unbounded range, in contrast to the sigmoid function which computes values in the 0-1 range to assist matching to a binary class. Additionally, we also constructed a 1D convolutional neural network (CNN) regression model which takes the raw time domain waveform data as the input and aims to predict AE signal's corresponding cycle number. The CNN consisted of two 1D convolutional layers, a flattened layer, and two dense layers, with the final layer using a linear activation function. However, both these models showed suboptimal regression performance as shown in **Figure S6**. Having tested various combinations of the neural network depth (number of layers including the output layer but excluding the input layer), width (maximum number of nodes in a layer), and kernel sizes (for the CNN), we found no significant improvement in the model's regression performance. This can further be explained by our unsupervised ML analysis. Applying the PCA and autoencoders to the long-term cycling dataset and observing whether the cycle number was related to clusters in the principal component or latent space, there was no clear relationship as shown in **Figure S8**.

The lack of clear relationship demonstrates that although our supervised ML models were able to distinguish between pristine and severely aged cells, representing the continuous evolution that takes place during degradation was more challenging. We believe that distinguishing between cells aging continuously is more intricate because degradation occurs gradually, resulting in subtle changes over time. Consequently, the waveforms generated may not have exhibited pronounced differences over each electrochemical cycle, making consistent model accuracy more difficult. Even if differences did exist, it is possible that the waveforms did not contain patterns that consistently evolved with progressive cycles. In contrast, the task for the aforementioned classification models, which attempted to classify cells with distinctly different age states, was comparatively easier. To address the challenge to regression, and to successfully correlate AE signals with the cycle number, the following avenues can

18

be considered. Firstly, data from additional cells could be processed, which would increase the size of each of the training, validation, and test sets to prevent overfitting. Additionally, exploring different ML or feature extraction techniques may be more successful in performing continuous predictions on SoH and cycle number and could be the focus of future work. Future work will involve conducting additional experiments with cells at different SoH, thereby creating a larger dataset. This expanded dataset will also enhance the performance and reliability of the ML model.
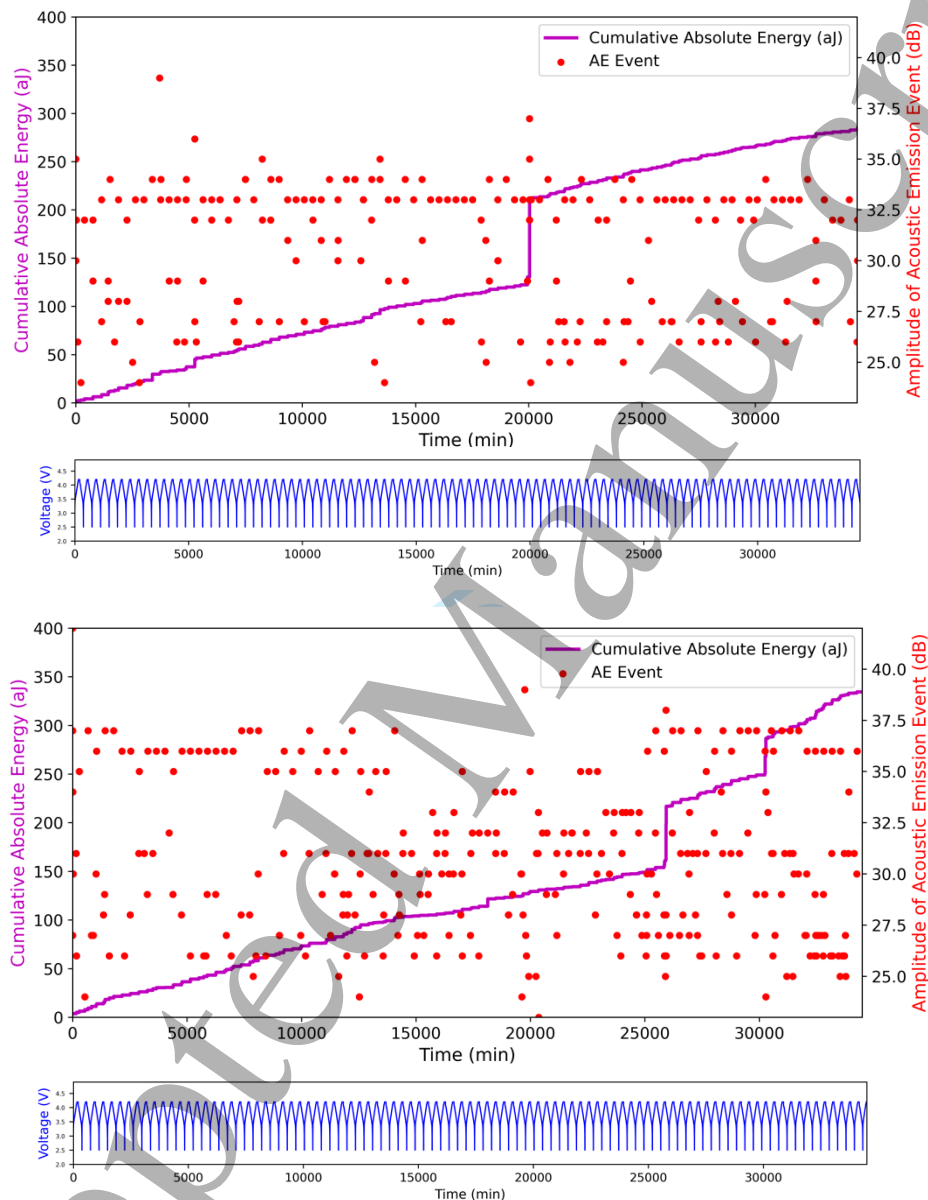

Figure 11. The amplitude of the acoustic hits is overlaid with cumulative absolute energy (CAE) for the pristine and aged cell (top and bottom, respectively). Each red dot corresponds to an acoustic hit of a particular amplitude. The blue plot below represents the charge and discharge curve of the cell while cycling between 2.5 and 4.2 V. Both cells were cycled at a C-rate of C/3 for 100 cycles.

4. Conclusion

The work demonstrated the importance of acoustic emission (AE) as a SoH diagnostic tool for cylindrical cells within LIB research. Through a bespoke experimental setup, both AE and electrochemical data were collected during cycling experiments on both pristine and aged cylindrical

19

LIBs at two different C rates (1C and C/3). AE analysis revealed that the occurrence of CAE jumps surpassing the 15 aJ threshold could be identified as a marker for differentiating pristine cell AE signals from those of aged cells. Longer term AE monitoring experiments provided further evidence that AE data can be used for distinguishing between the type and state of health (SoH) of cylindrical cells. To automate this signal identification process, Logistic Regression, Support Vector Machines (SVM), and Deep Neural Network (DNN) supervised Machine Learning models were employed, with the DNN model achieving an impressive accuracy of 93.8%. To mitigate the risk of overfitting, data was collected from three distinct AE sensor positions across the cell. Additionally, leveraging two k-means clustering models facilitated by Principal Component Analysis (PCA) and autoencoders, waveforms were successfully categorised based on their acoustic properties. This demonstration not only establishes the potential for rapid correlation of AE signals with degradation phenomena but also promises deeper insights for more accurate in-situ diagnostics. Furthermore, X-ray Computed Tomography (CT) measurements served to corroborate the degradation observed in the aged cells, providing compelling evidence that alterations in internal structure were the likely culprits behind the divergent acoustic signals. The integration of AE data with both supervised and unsupervised ML analyses presents a potent methodology for characterising the SoH of cylindrical LIBs, relying solely on acoustic information. This holds particular significance as acoustic techniques offer a cost-effective and non-destructive means to monitor the widely deployed cylindrical LIBs. In continuation of this work, developing a ML approach that uses AE data to estimate SoH on a continuous scale as discussed in Section 3.5, as opposed to binary classification, would allow for more nuanced diagnostics and greater practical applicability.

5. References

1.   International, I.E.A., and Agency, E. (2023). Global EV Outlook 2023.

2.   Conzen, J., Lakshmipathy, S., Kapahi, A., Kraft, S., and DiDomizio, M. (2023). Lithium ion battery energy storage systems (BESS) hazards. J. Loss Prev. Process Ind. *81*, 104932. 10.1016/j.jlp.2022.104932.

3.   Huang, J., Shen, W., and Lu, G. (2023). Mechanism of failure behaviour and analysis of 18650 lithium-ion battery under dynamic loadings. Eng. Fail. Anal. *153*, 107588. 10.1016/j.engfailanal.2023.107588.

4.   Zhong, H., Zhong, Q., Yang, J., and Zhong, S. (2022). Thermal behavior and failure mechanisms of 18650 lithium ion battery induced by overcharging cycling. Energy Reports *8*, 7286–7296. 10.1016/j.egyr.2022.05.183.

5.   Tang, W., Tam, W.C., Yuan, L., Dubaniewicz, T., and Soles, J. Estimation of the critical external heat leading to the failure of lithium-ion batteries. *26650*, 1–22.

6.   Chombo, P.V., and Laoonual, Y. (2022). Quantification of heat energy leading to failure of 18650 lithium-ion battery abused by external heating. J. Loss Prev. Process Ind. *79*, 104855. 10.1016/j.jlp.2022.104855.

7.   Liu, C., Neale, Z.G., and Cao, G. (2016). Understanding electrochemical potentials of cathode materials in rechargeable batteries. Mater. Today *19*, 109–123. 10.1016/j.mattod.2015.10.009.

8.   Wilfred Chan (2023). Four more people just died in an e-bike fire. If nothing changes, they won't be the last. Guardian. https://www.theguardian.com/us-news/2023/jun/22/ebike-battery-

fire-new-york-gig-workers.

9.   Jordyn Beazley (2023). Five cars destroyed at Sydney airport after luxury electric vehicle's battery ignites. Guardian. https://www.theguardian.com/australia-news/2023/sep/12/five-cars-destroyed-at-sydney-airport-after-luxury-electric-vehicles-battery-ignites.

10.   Ash-Har Quaraishi, Aparna Zalani, Ryan Beard, Dilcia Mercedes, D.M. (2023). Lithium-ion battery fires from electric cars, bikes and scooters are on the rise. Are firefighters ready? https://www.cbsnews.com/news/lithium-ion-battery-fires-electric-cars-bikes-scooters-firefighters/.

11.   Majasan, J.O., Robinson, J.B., Owen, R.E., Maier, M., Radhakrishnan, A.N.P., Pham, M., Tranter, T.G., Zhang, Y., Shearing, P.R., and Brett, D.J.L. (2021). Recent advances in acoustic diagnostics for electrochemical power systems. JPhys Energy *3*. 10.1088/2515-7655/abfb4a.

12.   Lamb, J., Orendorff, C.J., Steele, L.A.M., and Spangler, S.W. (2015). Failure propagation in multi-cell lithium ion batteries. J. Power Sources *283*, 517–523. 10.1016/j.jpowsour.2014.10.081.

13.   Rosengren, M. (2019). SAFETY & TRANSPORT FIRE RESEARCH Fire Safety of Lithium-Ion Batteries in Road Fire Safety of Lithium-Ion Batteries in Road.

14.   Sergei Klebnikov (2020). Elon Musk Is Nearly $10 Billion Richer This Week With Tesla On The Verge Of Joining The S&P 500. Forbes. https://www.forbes.com/sites/sergeiklebnikov/2020/12/19/elon-musk-is-nearly-10-billion-richer-this-week-with-tesla-on-the-verge-of-joining-the-sp-500/?sh=63b76ccb6d00.

15.   Bankole, O.E., and Lei, L. (2017). Battery Recycling Technologies : Recycling Waste Lithium Ion Batteries with the Impact on the Environment In-View. 10.5296/jee.v4i1.3257.

16.   Hsieh, A.G., Bhadra, S., Hertzberg, B.J., Gjeltema, P.J., Goy, A., Fleischer, J.W., and Steingart, D.A. (2015). Electrochemical-acoustic time of flight: In operando correlation of physical dynamics with battery charge and health. Energy Environ. Sci. *8*, 1569–1577. 10.1039/c5ee00111k.

17.   Linden, D., and Reddy, T.B. HANDBOOK OF BATTERIES.

18.   Gao, J., Lyu, Y., and He, C. (2022). Estimating State of Charge of Lithium-ion Batteries by Using Ultrasonic Guided Waves Detection Technology. J. Phys. Conf. Ser. *2198*. 10.1088/1742-6596/2198/1/012015.

19.   Komagata, S., Kuwata, N., Baskaran, R., Kawamura, J., Sato, K., and Mizusaki, J. (2010). Detection of Degradation of Lithium-Ion Batteries with Acoustic Emission Technique. ECS Trans. *25*, 163–167. 10.1149/1.3334804.

20.   Zhang, K., Yin, J., and He, Y. (2021). Acoustic Emission Detection and Analysis Method for Health Status of Lithium Ion Batteries. 1–17.

21.   Hao, W., Yuan, Z., Xu, Y., Zhu, S., Chen, H., and Fang, D. (2019). Damage analysis of cylindrical lithium-ion cells under three-points bending using acoustic emission. J. Power Sources *444*, 227323. 10.1016/j.jpowsour.2019.227323.

22.   Hao, W., Yuan, Z., Li, D., Zhu, Z., and Jiang, S. (2021). Study on mechanical properties and failure mechanism of 18650 Lithium-ion battery using digital image correlation and acoustic emission. J. Energy Storage *41*. 10.1016/j.est.2021.102894.

23.   Tang, C., Yuan, Z., Liu, G., Jiang, S., and Hao, W. (2020). Acoustic emission analysis of 18,650 lithium-ion battery under bending based on factor analysis and the fuzzy clustering method. Eng. Fail. Anal. *117*. 10.1016/j.engfailanal.2020.104800.

24.   Fordham, A., Milojevic, Z., Giles, E., Du, W., Owen, R.E., Michalik, S., Chater, P.A., Das,

21

P.K., Attidekou, P.S., Lambert, S.M., et al. (2023). Correlative non-destructive techniques to investigate aging and orientation effects in automotive Li-ion pouch cells. Joule *7*, 2622–2652. 10.1016/j.joule.2023.10.011.

25. Robinson, J.B., Owen, R.E., Kok, M.D.R., Maier, M., Majasan, J., Braglia, M., Stocker, R., Amietszajew, T., Roberts, A.J., Bhagat, R., et al. (2020). Identifying Defects in Li-Ion Cells Using Ultrasound Acoustic Measurements. J. Electrochem. Soc. *167*, 120530. 10.1149/1945-7111/abb174.

26. Ladpli, P., Kopsaftopoulos, F., Nardari, R., and Chang, F.-K. (2017). Battery charge and health state monitoring via ultrasonic guided-wave-based methods using built-in piezoelectric transducers. In Smart Materials and Nondestructive Evaluation for Energy Systems 2017 (SPIE), p. 1017108. 10.1117/12.2260107.

27. Owen, R.E., Robinson, J.B., Weaving, J.S., Pham, M.T.M., Tranter, T.G., Neville, T.P., Billson, D., Braglia, M., Stocker, R., Tidblad, A.A., et al. (2022). Operando Ultrasonic Monitoring of Lithium-Ion Battery Temperature and Behaviour at Different Cycling Rates and under Drive Cycle Conditions. J. Electrochem. Soc. *169*, 040563. 10.1149/1945-7111/ac6833.

28. Etiemble, A., Idrissi, H., and Roue, L. (2012). On the use of the acoustic emission technique for in-situ monitoring of the pulverization of battery electrodes. J. Acoust. Emiss. *30*, 54–64.

29. Tranchot, A., Idrissi, H., Thivel, P.X., and Roué, L. (2016). Influence of the Si particle size on the mechanical stability of Si-based electrodes evaluated by in-operando dilatometry and acoustic emission. J. Power Sources *330*, 253–260. 10.1016/j.jpowsour.2016.09.017.

30. Choe, C.Y., Jung, W.S., and Byeon, J.W. (2015). Damage evaluation in lithium cobalt oxide/carbon electrodes of secondary battery by acoustic emission monitoring. Mater. Trans. *56*, 269–273. 10.2320/matertrans.M2014396.

31. Bond, T., Gauthier, R., Eldesoky, A., Harlow, J., and Dahn, J.R. (2022). In Situ Imaging of Electrode Thickness Growth and Electrolyte Depletion in Single-Crystal vs Polycrystalline LiNixMnyCozO 2 /Graphite Pouch Cells using Multi-Scale Computed Tomography . J. Electrochem. Soc. *169*, 020501. 10.1149/1945-7111/ac4b83.

32. Tranchot, A., Etiemble, A., Thivel, P.X., Idrissi, H., and Roué, L. (2015). In-situ acoustic emission study of Si-based electrodes for Li-ion batteries. J. Power Sources *279*, 259–266. 10.1016/j.jpowsour.2014.12.126.

33. Schweidler, S., Dreyer, S.L., Breitung, B., and Brezesinski, T. (2021). Operando acoustic emission monitoring of degradation processes in lithium-ion batteries with a high-entropy oxide anode. Sci. Rep. *11*, 1–8. 10.1038/s41598-021-02685-2.

34. Schweidler, S., Dreyer, S.L., Breitung, B., and Brezesinski, T. (2022). Acoustic Emission Monitoring of High-Entropy Oxyfluoride Rock-Salt Cathodes during Battery Operation. Coatings *12*, 402. 10.3390/coatings12030402.

35. Martemianov, S., Maillard, F., Thomas, A., Lagonotte, P., and Madier, L. (2016). Noise diagnosis of commercial Li-ion batteries using high-order moments. Russ. J. Electrochem. *52*, 1122–1130. 10.1134/S1023193516120089.

36. Jnawali, A., Radhakrishnan, A.N.P., Kok, M.D.R., Iacoviello, F., Brett, D.J.L., and Shearing, P.R. (2022). Motion-enhancement assisted digital image correlation of lithium-ion batteries during lithiation. J. Power Sources *527*, 231150. 10.1016/j.jpowsour.2022.231150.

37. Kok, M.D.R., Jnawali, A., Heenan, T.M.M., Tranter, T.G., Brett, D.J.L., Shearing, P.R., and Robinson, J.B. (2023). Tracking the Lifecycle of a 21700 Cell: A 4D Tomography and Digital Disassembly Study. J. Electrochem. Soc. *170*, 090502. 10.1149/1945-7111/acf412.

38. Chang, W., Mohr, R., Kim, A., Raj, A., Davies, G., Denner, K., Park, J.H., and Steingart, D.

22

(2020). Measuring effective stiffness of Li-ion batteries: Via acoustic signal processing. J. Mater. Chem. A *8*, 16624–16635. 10.1039/d0ta05552b.

39. Kok, M.D.R., Robinson, J.B., Weaving, J.S., Jnawali, A., Pham, M., Iacoviello, F., Brett, D.J.L., and Shearing, P.R. (2019). Virtual unrolling of spirally-wound lithium-ion cells for correlative degradation studies and predictive fault detection. Sustain. Energy Fuels *3*, 2972–2976. 10.1039/c9se00500e.

40. Nadimpalli, S.P.V., Sethuraman, V.A., Abraham, D.P., Bower, A.F., and Guduru, P.R. (2015). Stress Evolution in Lithium-Ion Composite Electrodes during Electrochemical Cycling and Resulting Internal Pressures on the Cell Casing. J. Electrochem. Soc. *162*, A2656–A2663. 10.1149/2.0341514jes.

41. Wang, X., Sone, Y., Segami, G., Naito, H., Yamada, C., and Kibe, K. (2007). Understanding Volume Change in Lithium-Ion Cells during Charging and Discharging Using In Situ Measurements. J. Electrochem. Soc. *154*, A14. 10.1149/1.2386933.

42. Finegan, D.P., Vamvakeros, A., Cao, L., Tan, C., Heenan, T.M.M., Daemi, S.R., Jacques, S.D.M., Beale, A.M., Di Michiel, M., Smith, K., et al. (2019). Spatially Resolving Lithiation in Silicon-Graphite Composite Electrodes via in Situ High-Energy X-ray Diffraction Computed Tomography. Nano Lett. *19*, 3811–3820. 10.1021/acs.nanolett.9b00955.

43. Kircheva, N., Genies, S., Brun-Buisson, D., and Thivel, P.-X. (2011). Study of Solid Electrolyte Interface Formation and Lithium Intercalation in Li-Ion Batteries by Acoustic Emission. J. Electrochem. Soc. *159*, A18–A25. 10.1149/2.045201jes.

44. Tranchot, A., Etiemble, A., Thivel, P.X., Idrissi, H., and Roué, L. (2015). In-situ acoustic emission study of Si-based electrodes for Li-ion batteries. J. Power Sources *279*, 259–266. 10.1016/j.jpowsour.2014.12.126.

45. Bommier, C., Chang, W., Li, J., Biswas, S., Davies, G., Nanda, J., and Steingart, D. (2020). Operando Acoustic Monitoring of SEI Formation and Long-Term Cycling in NMC/SiGr Composite Pouch Cells. J. Electrochem. Soc. *167*, 020517. 10.1149/1945-7111/ab68d6.

46. MATSUO, T., UCHIDA, M., and CHO, H. (2011). Development of Acoustic Emission Clustering Method to Detect Degradation of Lithium Ion Batteries. J. Solid Mech. Mater. Eng. *5*, 678–689. 10.1299/jmmp.5.678.

47. Fukushima, T., Kato, S., Kuwata, N., and Kawamura, J. (2014). In-Situ Acoustic Emission Study of Sn Anode in Li Ion Battery. ECS Trans. *62*, 215–222. 10.1149/06201.0215ecst.

48. Gauthier, R., Luscombe, A., Bond, T., Bauer, M., Johnson, M., Harlow, J., Louli, A., and Dahn, J.R. (2022). How do Depth of Discharge, C-rate and Calendar Age Affect Capacity Retention, Impedance Growth, the Electrodes, and the Electrolyte in Li-Ion Cells? J. Electrochem. Soc. 10.1149/1945-7111/ac4b82.

23